



Effect of cyclic softening and mean stress relaxation on fatigue crack initiation in a hemispherical notch

Paul Qvale¹  | Ershad P. Zarandi¹ | Alberto Arredondo² | Sigmund K. Ås³  | Bjørn H. Skallerud¹

¹Department of Structural Engineering, Norwegian University of Science and Technology (NTNU), Richard Birkelandsvei 1A, NO-7491, Trondheim, Norway

²Vicinay Marine Innovación, Plaza Ibaiondo 1, planta 1a, Leioa, ES-48940, Spain

³Department of Marine Technology, NTNU, Trondheim, NO-7491, Norway

Correspondence

Paul Qvale, Department of Structural Engineering, Norwegian University of Science and Technology (NTNU), Richard Birkelandsvei 1A, NO-7491 Trondheim, Norway.
Email: paul.qvale@ntnu.no

Funding information

Norges Forskningsråd

Abstract

Corroded surfaces of offshore mooring chains typically show a very irregular shape with different pit geometries. Fatigue tests were performed in three-point bending on specimens with hemispherical notches, representing an idealized geometry of a corrosion pit. Digital image correlation was used to detect crack initiation lives and locations. The aim of the study was to quantify mean stress relaxation (MSR) and its influence on fatigue initiation life. MSR data were obtained from strain-controlled fatigue tests on R4-grade offshore mooring chain steel. Interestingly, MSR was observed even at a stress amplitude below the cyclic yield stress. For initiation lives below 100,000 cycles, significant improvement in predictions was obtained if cyclic softening and MSR were accounted for. Using only the monotonic stress-strain curve led to less accurate predictions. For longer lives, scatter in the base material *S-N* data and residual stresses from machining of the notch made predictions less accurate.

KEYWORDS

cyclic softening, digital image correlation, fatigue crack initiation, finite element, mean stress relaxation, offshore engineering

1 | INTRODUCTION

The structural integrity of offshore mooring chains is essential for safe operation of floating structures used for oil and gas extraction, wind energy production, and aquaculture. In order to accurately predict fatigue or corrosion fatigue lives of the chains, a good understanding of the material's cyclic stress-strain response is needed. A recent study by Zarandi and Skallerud¹ documented that strain-

controlled load cycling of R4-grade mooring chain steel at initial stress amplitudes above its monotonic yield stress, $R_{p0.2}$, can significantly alter its stress-strain response. The material exhibited *cyclic softening* and *mean stress relaxation* (MSR)—effects that are often neglected in fatigue calculations.

If fatigue loading is high enough to cause cyclic plasticity, most metals exhibit either cyclic hardening or softening.² Materials that have been work hardened tend to soften.^{2,3} Some materials have been reported to soften at low strain ranges and harden at high strain ranges.^{4–6}

Manuscript submitted for review to *Fatigue & Fracture of Engineering Materials & Structures* April 29, 2022.

This is an open access article under the terms of the [Creative Commons Attribution](https://creativecommons.org/licenses/by/4.0/) License, which permits use, distribution and reproduction in any medium, provided the original work is properly cited.

© 2022 The Authors. *Fatigue & Fracture of Engineering Materials & Structures* published by John Wiley & Sons Ltd.

The material response during cyclic plastic loading is governed by dislocation movements and the interaction between dislocations and the microstructure. Residual stresses that are present prior to cyclic plastic loading will relax by converting the elastic residual strains into microstructural plastic strains.⁷ This mechanism can also lead to *cycle-dependent* MSR during non-symmetric (stress ratio $R \neq -1$) strain-controlled cyclic loading and ratcheting during stress-controlled loading.^{3,8} It has been assumed that cyclic plastic straining is a prerequisite for MSR to occur.^{3,5,9} However, significant MSR has been reported for mild steel at stress amplitudes of around $R_{p0.2}/3$.⁶

Neglecting MSR effects in fatigue life predictions may lead to non-conservative predictions if initially compressive stresses are assumed to exist throughout the life. Current models used to calculate MSR^{10,11} can be somewhat physically based, in that they consider the evolution of yield surfaces and backstresses in a material continuum^{10,11} or the amount of cold work.¹² However, it has been demonstrated that the former models often overestimate the amount of ratcheting or MSR.¹⁰ Recent models have been developed to try to remedy this.¹³ However, accurate MSR models are still lacking in commercial FEA codes.¹⁴ Other MSR models^{6,15,16} are purely empirically based, simply fitting an expression to the measured shift of mean stresses as a function of the number of load cycles. It can be argued that a model with a physical basis is more likely to be adaptable to a variety of conditions. However, cycle-by-cycle FEA for calculating the evolution of relevant stress tensors for a whole component is often impractical due to the high computational cost.

Offshore mooring chains are subject to general and microbiologically influenced corrosion attacks.^{17,18} During cyclic loading, corrosion pits act as stress raisers, and may become initiation sites for corrosion fatigue cracks.¹⁸ The current work aims to improve the understanding of MSR and its influence on fatigue initiation. Since corrosion pits vary in size and shape,¹⁹ machined, hemispherical notches are considered here in order to develop a

generic approach for MSR in R4-grade steel chains. This simplification is consistent with a previous study of local strains around corrosion pits.¹ Some studies using physically based MSR and ratcheting models in stress-strain calculations for cyclically loaded notches exist.^{8,20,21} However, results of such calculations are not as easily verified as for smooth specimens.

In the current work, the transient stress-strain response, specifically cyclic softening and MSR, was calculated based on low-cycle fatigue results from Zarandi and Skallerud¹ and a complementary fatigue test performed at a lower strain level. A proposed MSR model was then used to predict fatigue initiation times and locations in hemispherical notches. Half of the specimens had compressive residual surface stresses, induced by an initial overload, to replicate the stress state found in a crown of an offshore mooring chain link.^{22,23} Fatigue initiation life and locations were verified from fatigue tests by continuous monitoring with digital image correlation (DIC).

2 | INVESTIGATION OF TRANSIENT STRESS-STRAIN RESPONSE IN R4-GRADE STEEL

Zarandi and Skallerud performed strain-controlled fatigue tests on R4-grade steel specimens extracted from the straight part (shank) of a mooring chain link.¹ It was found that the monotonic and cyclic stress-strain curve for the material can be described by the Ramberg-Osgood (RO) relation,

$$\varepsilon = \frac{\sigma}{E} + \left(\frac{\sigma}{K}\right)^{1/n}, \quad (1)$$

with parameters as noted in Table 1. σ denotes the stress, and ε denotes the strain. Parameters in Table 1 for monotonic loading were derived from a single stress-strain test, while parameters for cyclic loading were based on eight tests performed at fully reversed loading (strain

TABLE 1 Ramberg-Osgood parameters identified for monotonic and cyclic loading R4-grade mooring chain steel¹

Parameter	Symbol	Monotonic loading	Cyclic loading (stabilized)	First load reversal
Strain hardening exponent	n	0.0463	0.0688	0.1397
Strain hardening coefficient/MPa	K	1124	966	3316
Elastic modulus/GPa	E	207	207 ^a	195
Yield stress/MPa	$R_{p0.2}$	843	630	N/A

Note: A provisional model for the first load reversal is included in the rightmost column.

^aIn the current work, the apparent strain range dependency on E that was measured at high strain ranges¹ was disregarded, and the value of E for monotonic loading was adopted to the cyclic material model.

ratio $R_\epsilon = -1$). Moreover, in three non-symmetrically loaded tests performed at strain amplitude $\epsilon_a = 0.0045$ and $R_\epsilon = -0.33$, $R_\epsilon = 0$ and $R_\epsilon = 0.33$, mean stresses were found to relax by more than 90% during the fatigue half-life of the specimens.¹ The rate of MSR was shown

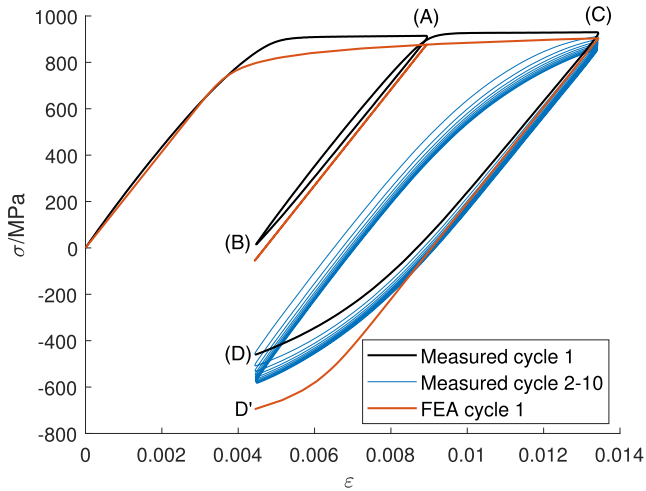


FIGURE 1 Stress-strain history for one of the non-symmetrically loaded tests ($\epsilon_a = 0.0045$, $R_\epsilon = 0.33$)¹ compared with FEA using the monotonic material model from Table 1. On execution of the test, the specimen was strained according to the following sequence: zero - mean (A) - minimum (B) - maximum (C) - minimum (D). Thereafter, the specimen was cycled between the strain levels of C and D until failure. The first 10 cycles are displayed [Colour figure can be viewed at wileyonlinelibrary.com]

to be highest during the first few cycles, an observation that is consistent with observations of MSR in other steels.^{2,5,13}

In Figure 1, the stress-strain response for the first cycle (black line) and the nine subsequent cycles (blue line) in one test are shown in more detail. Also shown are results from elastoplastic finite element analysis (FEA) using the monotonic material model from Table 1 with kinematic hardening. While the maximum stress (point C) in the first cycle is reasonably well replicated by FEA, there is a discrepancy between the measured (D) and calculated (D') minimum stress. This is caused by instant softening that manifests itself as non-Masing behavior.^{1,24} Using the computed stress values at point C and D' directly in fatigue calculations would yield large errors in mean stress estimates. However, it was observed that the stress-strain curves for the first load reversal (C to D) for all values of R_ϵ had almost identical shapes, indicating that the unloading behavior was independent of the magnitude of the maximum strain. Thus, as an alternative to the Masing model, a RO relation with parameters given in Table 1 could be fitted to the unloading curve by least-squares regression (with coefficient of determination, $R^2 = 0.9976$). This then provides a much better estimate for the initial mean stress, which is the basis for the MSR calculation described in Section 3.2.2.

For the non-symmetrically loaded tests by Zarandi and Skallerud,¹ Figures 2 and 3 show the evolution in the

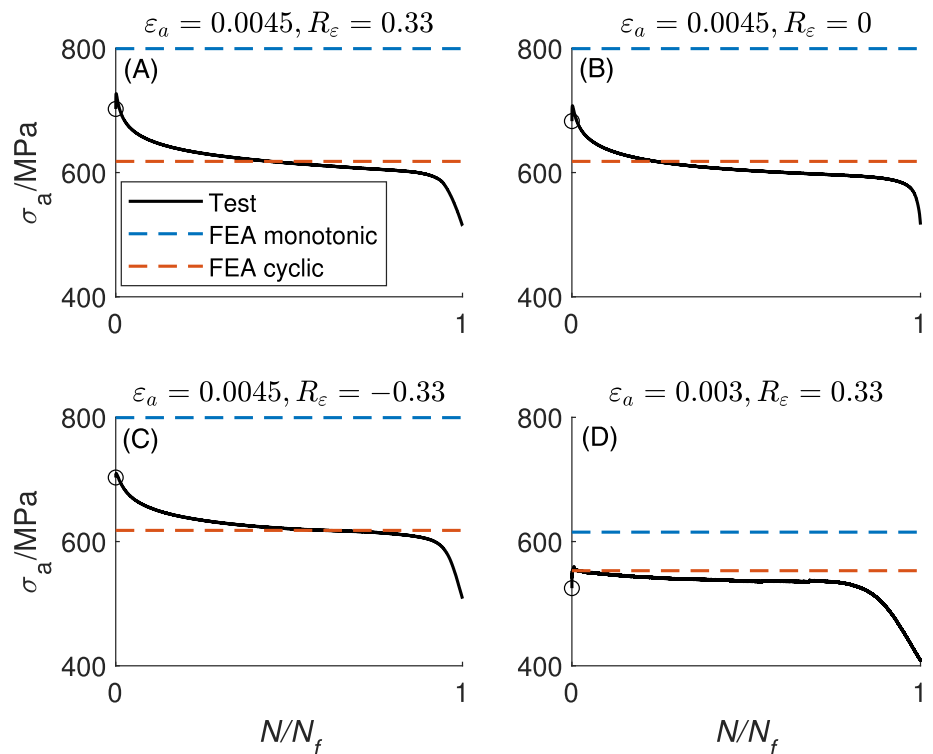


FIGURE 2 Measured stress amplitudes through the fatigue lives of specimens from Zarandi and Skallerud¹ and the current work, compared with FEAs using the monotonic and cyclic material models [Colour figure can be viewed at wileyonlinelibrary.com]

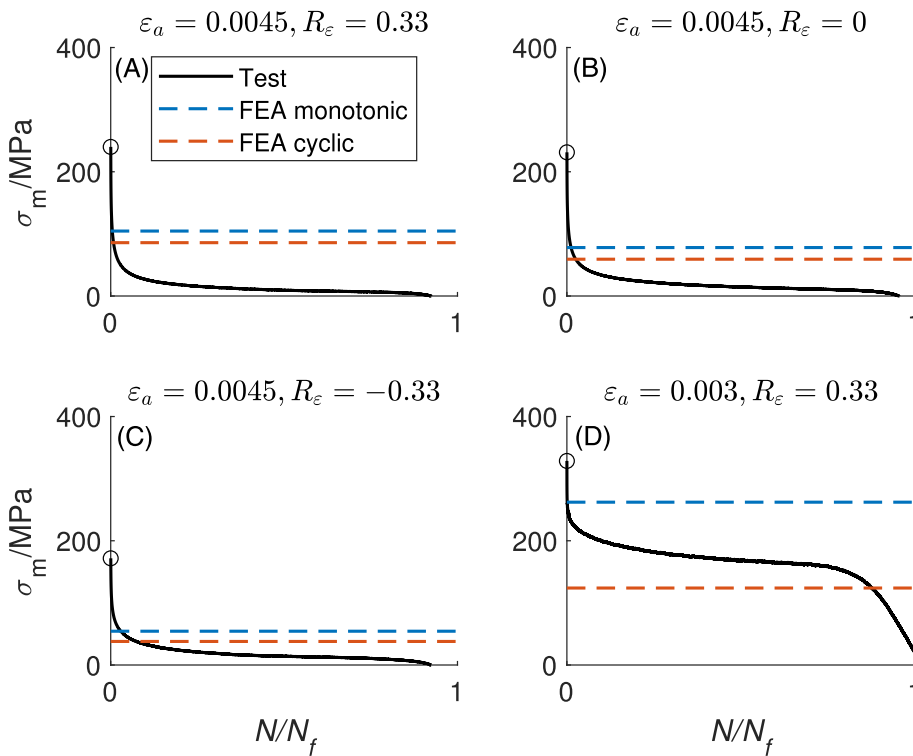


FIGURE 3 Measured mean stresses through the fatigue lives of specimens from Zarandi and Skallerud¹ and the current work, compared with FEAs using the monotonic and cyclic material models [Colour figure can be viewed at wileyonlinelibrary.com]

Element	C	Mn	Cr	Ni	Mo	Si	Fe and minor constituents
Percentage	0.24	1.3	1.3	0.7	0.3	0.3	Balance

TABLE 2 Chemical composition measured in chain links from the same production batch as the specimens were extracted from

stress amplitude, σ_a , and mean stress, σ_m , as a function of the ratio between the elapsed number of cycles, N , and the failure life, N_f . One additional test was made in the current work at a lower strain amplitude, $\varepsilon_a = 0.003$, and $R_\varepsilon = 0.33$ to complement the previous tests. The test setup was identical to that described by Zarandi and Skallerud,¹ except that the load frequency was 0.5 Hz, the wave shape was sinusoidal, and an Instron 100 kN servo-hydraulic machine was used. From Figure 3D, 49% MSR at half-life can be identified for the specimen run at $\varepsilon_a = 0.003$. The strain amplitude corresponds to an elastically calculated $\sigma_a = 621$ MPa, which means there is significant MSR at a stress amplitude well below the monotonic yield stress of the material (cf. Table 1). Moreover, the blue dashed lines in Figure 2 confirm that σ_a for the first load cycle cannot be calculated accurately for any of the tests by using the monotonic material model in an FEA. However, the red lines show that the cyclic material model can adequately represent the stabilized stress amplitude. Regarding the mean stress, neither the initial nor the stabilized value is well represented by any of the two models without correction.

3 | FATIGUE TESTING OF SPECIMENS WITH HEMISPHERICAL NOTCHES

3.1 | Experimental setup

3.1.1 | Specimen preparation

For the study on hemispherical notches, eight specimens were extracted near-surface from the non-welded shanks of two connected $\text{Ø}114$ mm mooring chain links made from R4-grade steel. The chain links had been processed according to standard specifications.²⁵ The chemical composition of chain links from the same production batch is given in Table 2. The tests by Zarandi and Skallerud were also conducted on material from a link from the same chain. The current fatigue testing was performed in conjunction with a study of fatigue initiation from natural corrosion pits¹⁹ and thus involved a chain that had been in service and submerged in sea water. The chain links had been in service on a floating production storage and offloading (FPSO) vessel for 20 years. The specimens

were cut from the chain links using electrical discharge machining (EDM) and then milled to their final dimensions shown in Figure 4. The coordinate system shown in the figure is used as a reference throughout this article. In half of the specimens, hereby referred to as the *as-machined* (AM) specimens, $\text{Ø}3$ mm hemispherical notches were drilled in the centers of the surfaces that had been facing outwards on the chain link. Before the notches were drilled in the other half of the specimens, one high loading-unloading cycle was applied to them to induce compressive residual surface stresses, as detailed in Section 3.1.2. These specimens are referred to as *pre-loaded* (PL) specimens. In the AM specimens, notches were drilled using a drill bit with a $\text{Ø}3$ mm hemispherical tip at 12,000 rpm and 180 mm/min feed rate. In the PL specimens, vibrations occurred during drilling when penetrating material with compressive residual stresses. To remedy this, the feed rate was reduced to just 0.2 mm/min, and the potentially dulled drill bit was replaced between drilling of each notch. After drilling, any remaining lips outside of the notches were removed by gently rubbing a #2000 grit sandpaper in the z direction.

3.1.2 | Preloading and fatigue setup

The PL specimens were first preloaded in three-point bending with a plastically deforming load and then unloaded. This resulted in a compressive residual stress field in the z direction opposite of the load surface.²⁶ The residual stress field was meant to represent that on the outside curved part (crown) of a proofloaded offshore mooring chain, where longitudinal residual stresses of -500 to -400 MPa had been measured close to the surface.²³

Figure 5 shows the rig used for preloading and fatigue loading. During preloading of the PL specimens, a 44 kN load was applied at the load cylinder. After unloading, an average residual stress in the z direction of -332 MPa was calculated from X-ray diffraction stress measurements directly opposite of the attack line of the load cylinder on one specimen. The stress measurements were performed using a Proto iXRD with a Cr cathode run at 20 kV and 4 mA, and a 1 mm diameter aperture. Proto

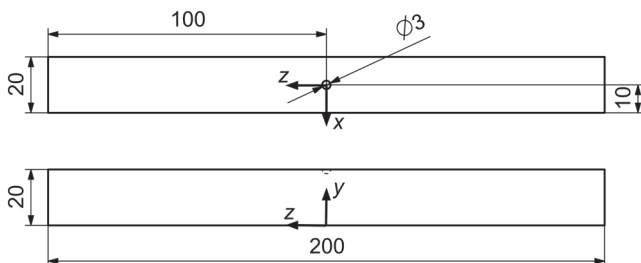


FIGURE 4 Fatigue testing specimen geometry

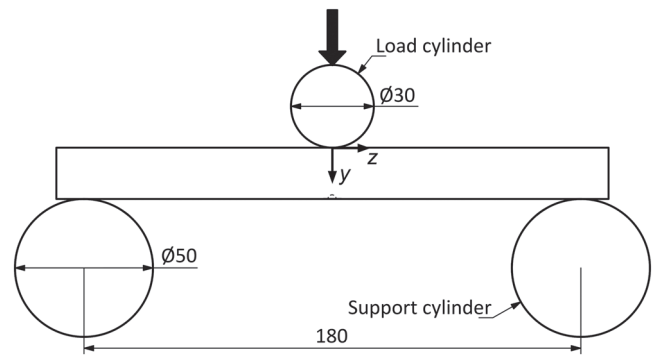


FIGURE 5 Schematic drawing of the three-point bending loading rig

XRDWIN software was used to analyze the result according to the $\sin^2\psi$ method using 11 beta angles ($\pm 20^\circ$). Elastoplastic FEA of the preloading was performed using the monotonic material model. Details about the FEA are provided in Section 3.2.1. Since the non-Masing behavior during unloading was not accounted for by the kinematic hardening model in the FEA (see Figure 1), Neuber's rule²⁷ was used to shift from the FEA result to the RO curve for first load reversal from Table 1. In good agreement with the measurements, a residual stress of -319 MPa was calculated.

The specimens then underwent cyclic loading according to Table 3. All load cycles had a load ratio of $R_L = 0.2$. The loads were applied using a triangular wave shape and a frequency of 3 Hz. Loading was applied using a calibrated Instron 8800 250 kN test system and an A10025E cylinder with a stroke of 250 mm.

It is apparent from Table 3 that the notch mean stress at the lowest load level was significantly lower in the PL specimen than in the AM specimen, because of the residual compressive stresses from preloading (e.g., compare results for specimens 1 and 5). For higher load levels, stress ranges were so high that maximum (and mean) stresses ended up at comparable levels. Minor differences in notch stress amplitudes between the AM and PL specimens in Table 3 at equivalent load levels were a result of plastic deformation of the contact surfaces with the load cylinder in the PL specimens during preloading. That is, the load cylinder had a larger contact surface for the PL specimens.

3.2 | Prediction of fatigue initiation life

3.2.1 | FEA model

FEA models with two symmetry planes were created in Abaqus 2017 for all specimens. Figure 6 shows the quadratic reduced integration (type C3D20R) element mesh. Doubling the element count along all axis directions for

TABLE 3 Load levels for each specimen

Specimen ID	Preloaded	Load amplitude (kN)	Mean load (kN)	Stress amplitude (MPa)	Mean stress (MPa)
1	No	8	12	479	407
2	No	8	12	479	407
3	No	10	15	569	340
4	No	12	18	638	292
5	Yes	8	12	467	135
6	Yes	10	15	558	306
7	Yes	12	18	628	349
8	Yes	14	21	678	334

Note: Surface stresses in z direction from the most highly stressed point (close to the mouth) in the notch are given. Calculations are performed by elastoplastic FEA using the monotonic material model and the RO relation for first load reversal. Stresses are valid for the first load cycle. Mean stresses include residual stresses.

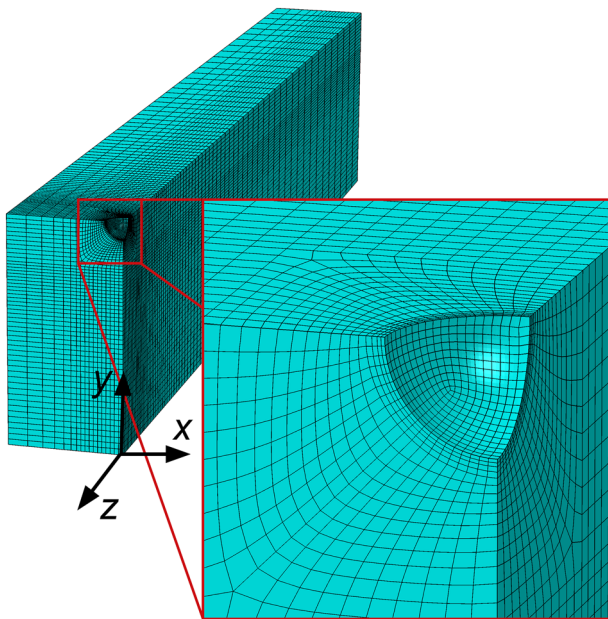


FIGURE 6 Mesh of FEA model [Colour figure can be viewed at wileyonlinelibrary.com]

one specimen resulted in less than 0.2% change in output values at the notch mouth. Thus, the original mesh was considered adequate for stress and strain representation.

It was assumed that all stresses from production of the chain links were completely relieved during specimen extraction. Thus, the specimens were modeled as initially stress-free.

“Hard,” normal contact was modeled between the specimen and the load cylinder in order to accurately represent the plastic response in the specimen midsections during preloading of the PL specimens. The model was configured to take into account geometric nonlinearities. To replicate the specimen preparation process, preloading was simulated on notch-free models, and elements inside the notches were deactivated before

fatigue loading was applied. Multilinear, kinematically hardening material models based on parameters from Table 1 were employed.

The post-processing of the FEA results to calculate fatigue initiation lives were performed in the numeric computing environment MATLAB. Procedures are detailed in the following section. In the calculations, both applied mean stresses and any residual stresses from preloading in the FEA results were considered as mean stresses.

3.2.2 | Fatigue initiation prediction

The highest stresses in Table 3 show that the test program extended into the low-cycle fatigue (LCF) domain. Therefore, strain-based fatigue initiation prediction, based on the Basquin²⁸ and Coffin-Manson^{29,30} equations, was deemed most appropriate. For the specimens with the lowest loads and limited plastic strains, this approach reduces to a stress-based one. To account for mean stresses, the model of Smith, Watson and Topper (SWT)³¹ was employed, resulting in the equation²

$$\sigma_{\max} \varepsilon_a = \frac{\sigma_f'^2}{E} (2N_i)^{2b} + \sigma_f' \varepsilon_f' (2N_i)^{b+m}. \quad (2)$$

Here, $\sigma_{\max} = \sigma_a + \sigma_m$ is the maximum stress during a load cycle. σ_f' and b are the Basquin parameters that signify the $N = 0.5$ intercept and the (negative) slope of an $S-N$ curve in a plot with logarithmic axes. ε_f' and m are equivalent Coffin-Manson parameters for an $\varepsilon_{\text{plastic}}-N$ curve. N_i is the number of cycles at fatigue crack initiation.

Stabilized stress and strain ranges to be used in the fatigue predictions were calculated at the notch surface using FEA and the cyclic material model with kinematic

hardening, since this model had shown in Figure 2 to give accurate representations. It can be argued that, as the load cycles are exerted on a specimen, the material will soften in regions where the stress amplitudes exceed the cyclic yield stress. Thus, the global cyclic response will approach that which can be represented by the cyclic material model.

In addition to the stress and strain ranges, an accurate estimate of the mean stresses is also needed to determine σ_{\max} in Equation (2). An estimate was achieved by firstly calculating the mean stress in the first load cycle, by using FEA with the monotonic material model and then adjusting the minimum stress by shifting to the RO relation for first load reversal. The shift was performed while keeping the strain constant, equivalent to moving from point D' to point D in Figure 1. Thereafter, a linear regression from Figure 7, based on the observations of MSR presented in Figure 3, was used to estimate the mean stress at half-life. Figure 7 shows the ratio of half-life mean stresses to initial mean stresses as a function of the strain range. Since mean stresses have been shown to quickly relax and approach more or less stable values, constant mean stresses equal to those at the half-lives were used in the fatigue predictions. Moreover, any resulting stress cycles with maximum or minimum values that exceeded the cyclic stress-strain curve, were adjusted accordingly.

It is widely accepted that fatigue initiation in components with steep stress gradients is not controlled solely by the highest surface stress amplitude.^{32,33} Several methods have been developed to take the subsurface

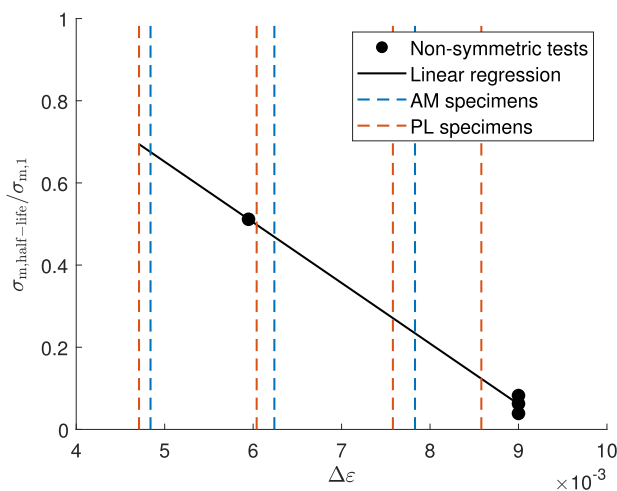


FIGURE 7 Linear regression model for the ratio of half-life mean stresses, $\sigma_{m,half-life}$, to initial mean stresses, $\sigma_{m,1}$, as a function of the strain range. Maximum strain ranges in the hemispherical notches, as well as results from the non-symmetrically loaded tests by Zarandi and Skallerud¹ and the current work have been plotted [Colour figure can be viewed at wileyonlinelibrary.com]

stress distribution into account.³² Taylor's point-based critical distance method³⁴ was adopted in the current work. Instead of evaluating the surface state in the notch, this method considers the stress and strain at some distance (related to the crack process zone) below the surface. Thus, in the notch, rather the subsurface than the surface stress was considered for the fatigue calculations. For locations in the notch, the critical distance was employed along the surface plane normals. The critical distance method was chosen because of its simple application to combined distributions of stress and strain. Moreover, an exhaustive review of fatigue tests on notched 30CrNiMo8 low-alloy steel specimens, showed that the method could provide reasonably accurate results for a variety of stress distributions.³²

In lack of stress gradient sensitivity investigations for R4-grade steel, the same critical distance as for the thoroughly reviewed 30CrNiMo8 was used in the current work, that is, $d = 34 \mu\text{m}$.³² Taylor has argued the critical distance of a material is related to its strength and grain size.³⁵ At 730–828 MPa³² and 20–40 μm ,^{36,37} the yield strength and grain size of 30CrNiMo8 is comparable to 843 MPa¹ and 15–25 μm measured for R4-grade steel. This provides some support to the claim that d should also be similar for the two materials. Stresses and strains at critical distance from the surface was found by linear interpolation between FEA element nodal values at and 50 μm below the surface.

At $d = 34 \mu\text{m}$ from the surface, calculated von Mises stress amplitudes deviated by less than 4.5% from the corresponding normal stress amplitudes within the top 30° from the notch mouth. This indicated low degree of multiaxiality in the stress states. Thus, little difference can be expected between alternative multiaxial stress criteria,³⁸ and the z -direction/normal stress and strain was conveniently used for the fatigue initiation analysis. In summary, Figure 8 shows the complete methodology for the fatigue prediction that was performed along the notch profile.

For the fatigue calculations, low-cycle and high-cycle $S-N$ data for R4-grade steel were collected from Zarandi and Skallerud¹ and Arredondo et al,³⁹ respectively. Some additional, previously unpublished data points from Arredondo's test program were included. It was assumed that the use of smooth, small-scale specimens in the referenced test programs promoted a high ratio of initiation to total fatigue life, so that the data could be used to predict initiation lives in the current notched specimens. At least for long fatigue lives, this should be a sound assumption. In addition to the $S-N$ data, $e'_f = 0.725$ and $c = -0.6508$ were obtained from Zarandi and Skallerud.¹

Figure 9 shows all raw data points from the test programs in blue and grey. In the figure, and throughout the

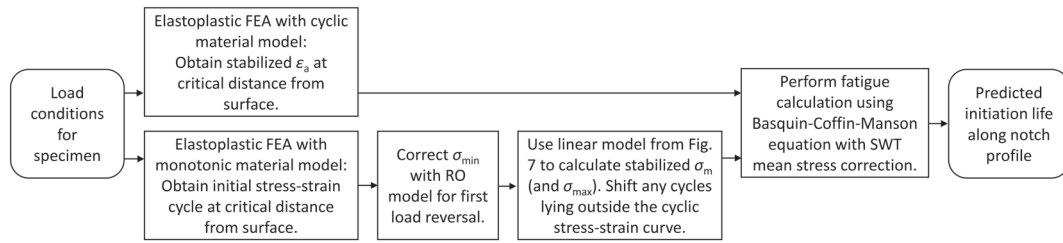


FIGURE 8 Flow chart for fatigue prediction methodology for the notched specimens

current work, arrows mark run-out tests—that is, tests where no failure occurred during the testing period. Zarandi and Skallerud's tests were run at stress ratio $R = -1$. Arredondo's tests were run at $R = 0.1$ and needed to be adjusted to $R = -1$ to produce correspondence. The inherent mean stress correction term of Equation (2), namely, $\sigma_{a,R=-1} = \sqrt{\sigma_{\max} \sigma_a}$, was used to adjust the data points.² The adjusted points are shown by red markers in Figure 9.

Maximum-likelihood regression^{19,40} was used to fit the most probable double-slope $S-N$ fatigue initiation curve to the adjusted data, accounting for both failed and run-out tests.[†] That is, the best fits of both slopes, as well as the knee point, were determined simultaneously by iteration over all possible configurations for the whole data set. The $S-N$ data was assumed to be Weibull distributed.⁴¹ To accommodate the apparent large scatter in N in the lower part of the data, the regression was performed by treating N as the independent parameter. The data point from Arredondo with the lowest stress amplitude ($\sigma_a = 232$ MPa for $R = 0.1$) was considered an outlier and was thus not included in the curve fitting.

3.3 | DIC measurements of fatigue crack initiation life

Fatigue crack initiation was defined as the first sign of a crack that could be detected by DIC. DIC is a full-field monitoring technique⁴² that has recently been employed to measure strain evolution around artificial corrosion pits⁴³ and crack initiation on naturally corroded surfaces¹⁹ during fatigue testing but has never been used inside hemispherical notches. For acquiring photographs, one camera was placed in the $x-y$ plane on each side of the specimen, at a 48° angle to the $x-z$ plane. This allowed

[†]Although the horizontal position of a run-out data point in an $S-N$ diagram is not defined, the run-out test suggests that the fatigue life is longer than the test duration, that is, that the $S-N$ curve is located to the right of the point. This information is considered in maximum-likelihood regression.

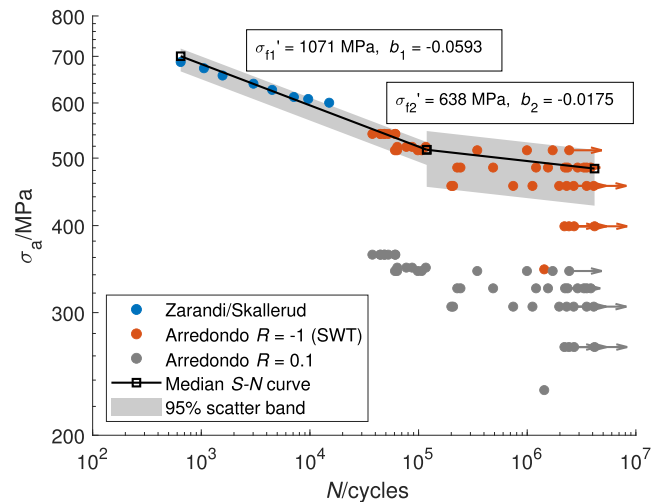


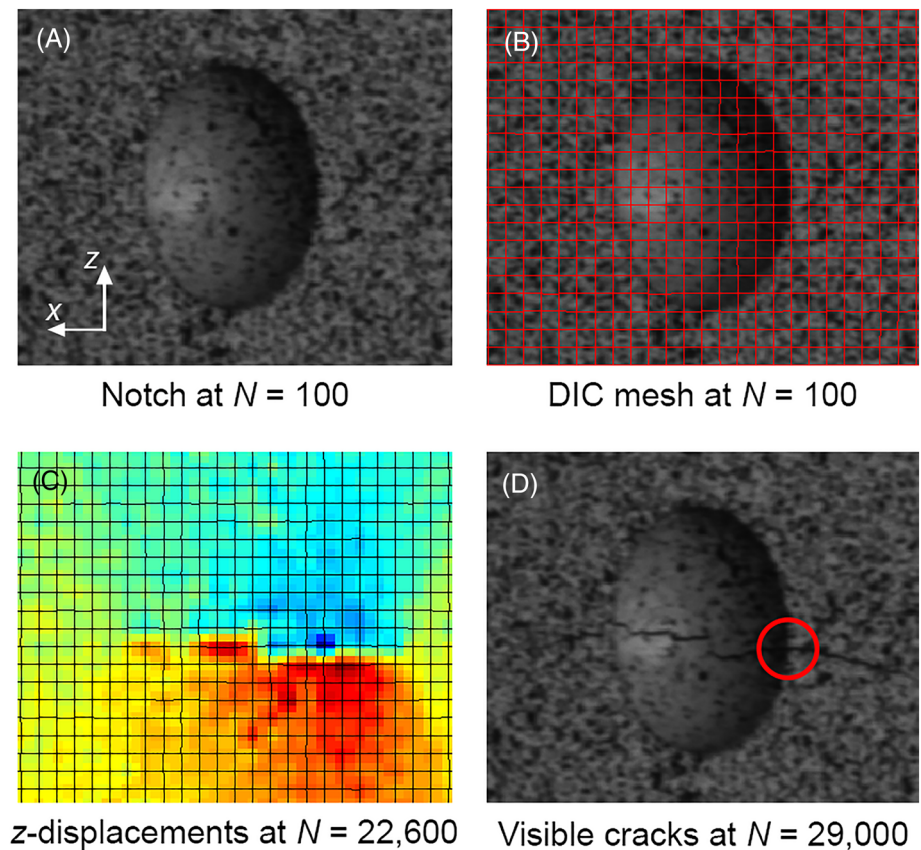
FIGURE 9 Double-slope $S-N$ curve for R4-grade steel and $R = -1$, constructed by maximum likelihood regression on data from Zarandi and Skallerud¹ and Arredondo et al.³⁹ SWT's mean stress criterion has been used to shift the raw data from Arredondo. Arrows mark run-out tests [Colour figure can be viewed at wileyonlinelibrary.com]

the whole $x-y$ plane surface profile of the notch of a specimen to be monitored. The DIC setup and crack detection criterion that were used in the current work are identical to those used by Qvale et al.¹⁹ The reader is referred to Qvale et al.¹⁹ for a detailed description of the camera setup, DIC mesh, crack detection methodology and possible error sources.

4 | RESULTS

Figure 10 shows photographs of the notch of specimen 4 for DIC processing. The applied mesh in Figure 10B was used to track movement of surface points and detect crack initiation according to the detection criterion in Coffin.¹⁹ Figure 10C shows a color plot of the displacement field in z direction for a crack that has grown past the mouth of a notch. Cracks at the initiation stage did not show up as distinct features in color plots but could be identified by tracking the inter-node displacements in MATLAB.

FIGURE 10 Crack development and DIC mesh for the notch in specimen 4. (A)–(D) all show the same section of the specimen. In (C), blue color shows positive displacements and red color shows negative displacements. In (D), the red circle shows the initiation location [Colour figure can be viewed at wileyonlinelibrary.com]



Crack surface lengths, $2c$, at the moment of detection could not be verified by other measurement techniques. Nevertheless, a crude estimate can be calculated based on FE solutions of Raju et al. for a semi-elliptical surface crack under bending load⁴⁴ and the current crack detection criterion, which signals a crack when the inter-node displacement across the crack plane reaches $2\ \mu\text{m}$.¹⁹ The solution for the shallowest crack of Raju et al. (still a relatively deep crack with a depth-to-plate-thickness ratio of $a/t=0.2$), when assuming $a/c=0.8$ and a bending surface stress equal to the cyclic yield stress, yields a crack of $2c=0.53\ \text{mm}$ for a crack mouth opening displacement of $2\ \mu\text{m}$.

Micrographs of all fracture surfaces where cracks initiated are shown in Appendix A (Figure A1). Specimen 8 was part of an individual study, and fatigue testing was stopped before final fracture.

Figure 11 shows the cycles to fatigue initiation registered by DIC, as well as the total fatigue lives, for all the tested specimens. It is apparent that at high load amplitudes the ratio of crack growth life to the total fatigue life is the highest. Two of the specimens tested at the lowest load level did not show any signs of fatigue initiation during the testing period. Moreover, the test at the highest load level was stopped after initiation, but before failure, for an independent fractographic study of the specimen.

Longer initiation lives were documented for the PL specimens than for the AM specimens.

Figure 12 shows the predictions for fatigue initiation lives compared to measurements by DIC. The results are also given in table form in Appendix B (Table B1) and marked on fracture surfaces in Appendix A. Blue, unfilled markers signify predictions where the cyclic material model and MSR have been taken into account. For the red markers, MSR has been neglected. Finally, for reference, grey markers show the outcome of calculations based directly on FEA results where the monotonic material model has been used without any further post-processing. Isolines of the ratio $r=N_{i,\text{predicted}}/N_{i,\text{measured}}$ give indications of the accuracy of the results. It is apparent that the blue markers are closest to the $r=1$ ideal line. Agreement is very good for $N_i < 10^5$ cycles. For higher N_i , all methods yield very conservative predictions. Reasons for the deviations are discussed in the next section. “Cyclic” and “Cyclic+MSR” predictions fall together for the low load levels, meaning that it is here predicted that the cyclic softening alone is controlling the mean stress relaxation.

In Figure 13, notch profiles in the x - y plane are displayed for all specimens. For each notch, fatigue initiation lives have been plotted on logarithmic axes normal to the profile. This way of presenting the results allows

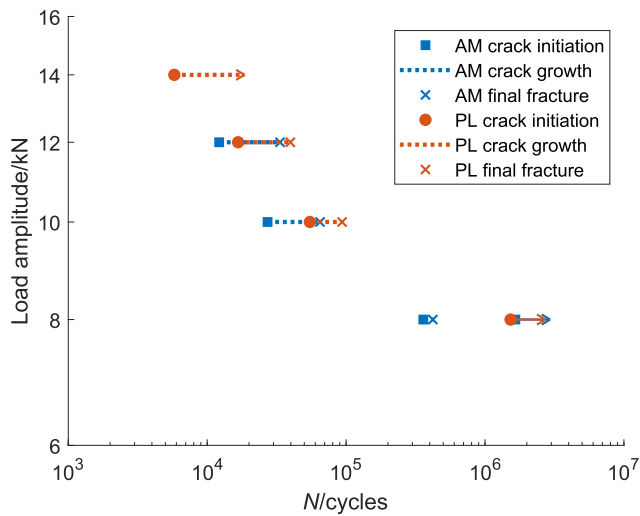


FIGURE 11 Measured numbers of cycles to fatigue initiation and failure for the notched specimens [Colour figure can be viewed at wileyonlinelibrary.com]

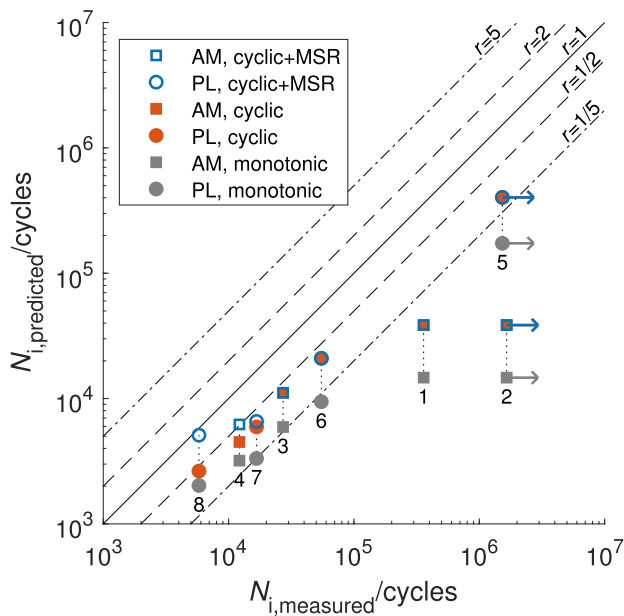


FIGURE 12 Predicted versus measured initiation lives for the notched specimens. “Cyclic” and “monotonic” refers to the respective material models used. Isolines of $r = N_{i,predicted}/N_{i,measured}$ are shown. The specimen numbers from Table 3 are printed below each vertical collection of points [Colour figure can be viewed at wileyonlinelibrary.com]

for easy identification of fatigue hotspots and initiation lives. The blue lines show the predicted initiation life distributions. Red dots show initiation locations and lives measured by DIC. Red error bars from a dot show the distance to neighboring DIC nodes, representing the surrounding region that is unmonitored and where the actual initiation could have occurred. Dashed red lines

show the test duration of run-out tests without any registered fatigue initiation.

DIC readings on some specimens exhibited independent cracks growing from both sides of the notch. For these specimens, both initiations are marked in the diagrams. In specimen 7, identical initiation lives were registered in two nodes on the right side. This indicates that a crack initiated between the two nodes. A lot of noise was observed in the DIC measurements for specimen 8 because of low gray levels in the photographs. Thus, the results for this specimen are somewhat less accurate. Overall, it seems that the (2D) DIC routine was adequate to identify and display realistic developments of fatigue cracks on the curved notch surfaces.

Predictions indicated that the most likely location for fatigue initiation was just below the notch mouth, at 9 to 36° below the surface. Such observations are in line with previous calculations of stress and strain concentrations in hemispherically notched specimens^{45,46} and mooring chain links.¹ Actual initiations were measured between 0.3 mm outside of the notch and 30° down in the notch and were in very good agreement with calculated locations. Variations in predicted initiation lives are generally small within the notch of one specimen. The exception is specimen 5, which is the only specimen with stresses in the bottom of the notch lying below the knee point of the $S-N$ curve.

5 | DISCUSSION

The current work has demonstrated by a fatigue test that mean stresses in R4-grade steel can relax by almost one half of the initial value at a stress amplitude well below the monotonic yield stress and just below the cyclic yield stress. This contradicts the suggestion that macroscopic plastic straining is needed for MSR to occur, as indicated by some authors for other materials.^{3,5,9} However, in the current work, the stress at 0.2% plastic strain, $R_{p0.2}$, is regarded as the yield stress. Further investigations are needed to determine the relationship between the onset of MSR and fatigue loading with very low plastic strains.

One could hypothesize that dislocations created during the initial uploading above the monotonic yield stress facilitates some cyclic plastic straining at lower stress amplitudes than the cyclic yield stress suggests. In Figure 1, an indication of macroscopic plasticity is the rapid deviation from elastic behavior at the first load reversal C-D. Even the initial, small cycle A-B-A exhibits a hysteresis loop, although the $\sigma_a = 450$ MPa is much lower than the cyclic yield stress of 630 MPa. The effect high mean strains on the cyclic material model should be investigated.

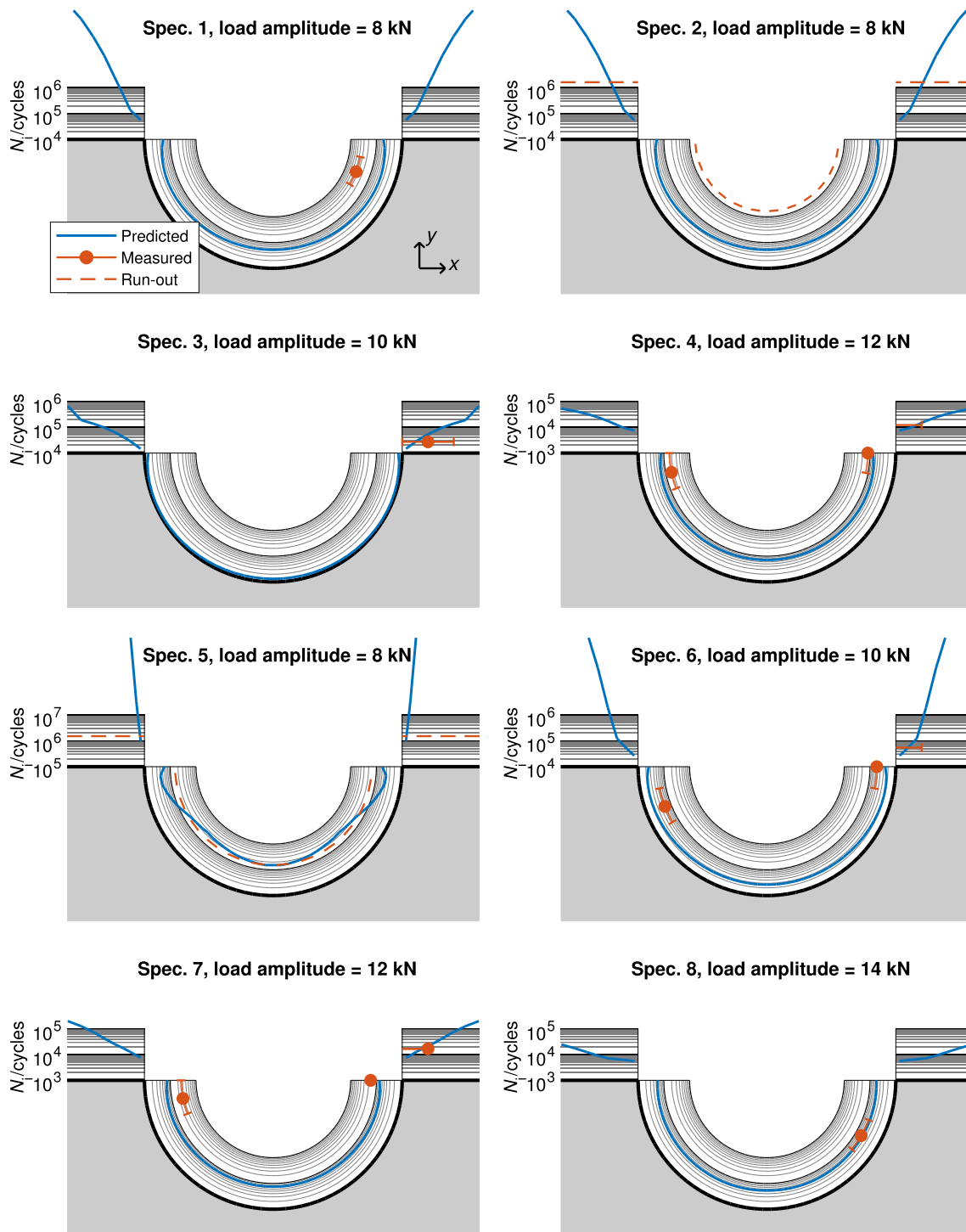


FIGURE 13 Predicted and measured fatigue initiation locations and lives at the notch profiles of all specimen. Specimens 1–4 and 5–8 are AM and PL specimens, respectively. Initiation lives have been predicted while accounting for cyclic softening and MSR [Colour figure can be viewed at wileyonlinelibrary.com]

The linear relation that was used to estimate the amount of MSR in the current work was based on measurements for only two strain ranges. It would probably have been possible to develop a more accurate model if test data from more strain ranges were available. Nevertheless, the amount of MSR that was observed should

encourage taking this effect into account when predicting fatigue lives, and the current relation offers one way of doing so.

Preferably, a physically based plasticity model that can take into account both the non-Masing behavior at the first load reversal and the successive transient

behavior should be developed. Such an approach would be more robust than the current empirical fits and also able to account for stress states with a higher degree of triaxiality. Some recent studies show promising results, but need more experimental verification.²⁰ The RO model for the first load reversal seemed to predict residual stresses with high accuracy in the PL specimens after the overload. However, for more complex load histories, the use of the model becomes less trivial and its applicability more questionable. A first step towards a model that is universally applicable and simpler to use could be to try to capture the kinematic hardening behavior during the first load cycle that is not accurately represented by the current FEA model.

In Figure 1, there are apparent deviations between the FEA using the monotonic material model and the measured stress-strain behavior, not only for the unloading. Inability of the FEA to follow the loading path from zero to point A, indicates that material parameters can vary, also within one single production batch. This may result in deviations in fatigue predictions. For more accurate predictions, monotonic material model parameters could be based on the average behavior from a broader database of tensile tests on chain link material from the same production batch.

For all the notched specimens, taking in account cyclic softening and MSR in fatigue predictions led to more accurate results. Prediction accuracy is high for $N_{i,measured} < 10^5$. For longer initiation lives, deviations increase. Some possible explanations are discussed below.

Machining has the potential to create shallow residual stresses, with magnitudes highly dependent on process parameters, and that can be either tensile or compressive in the depth range of the estimated critical distance.^{47–50} In the notched specimens, one can assume that the tangential feed motion of the ball end drill bit with respect to the notch mouth, or the very low feed rate used for drilling in the PL specimens, led to nonoptimal cutting conditions and aggravation of the residual stress state in the hot spots for fatigue initiation. It can be shown by geometric calculations that the current drilling parameters yields a cutting depth of only 17 nm per revolution at the bottom of the notch, and 3 nm at 10 degrees from the mouth of the notch. For high load levels, the shallow residual machining stresses may have been redistributed and effectively removed by the first loading. For the low load levels, cyclic stresses might not have been high enough to induce plastic straining in regions of high, compressive residual machining stresses (since the maximum surface stress amplitudes are below the cyclic yield stress, cf. Tables 1 and 3). Thus, the machining stresses might have altered the effective mean

stresses and been a major contributor to the observed deviations at long fatigue lives.

The scatter (in N) in the data in Figure 9 increases greatly when approaching the knee point of the $S-N$ curve from the high σ_a side. Moreover, Lassen et al.⁵¹ document $S-N$ data points for $R=0.1$ loading of R4 steel that are even deviating from those of Arredondo. In addition to the scatter, comes the uncertainty of using an empirical relation to correct non-symmetric stress cycles to equivalent symmetric ones. Stress amplitudes in the hemispherical notches at the lowest load levels lie quite close to the knee point, and the high scatter makes accurate prediction of initiation lives of single specimens challenging. Fatigue testing a larger number of hemispherically notched specimens at one load level would have yielded a measure of the scatter among these and allowed for a clearer comparison of predicted and measured initiation lives. Moreover, the gradual transition in the scatter around the knee point is not well represented by the current $S-N$ curve model. Moreover, the shallow slope that is predicted for the lower part of the $S-N$ curve might indicate that the stress amplitudes are close to the fatigue limit.

The increasing scatter in lower part of the $S-N$ curve in Figure 9 gives rise to a considerable size effect. That is, the probability of initiation in a specimen increases if the highly stressed region is enlarged. The area of a notch that had stress amplitudes above 90% of the highest one was around two orders of magnitude smaller than the homogeneously stressed area on specimens that the $S-N$ curve was constructed from. Taking the size of the stressed area into account would thus result in longer predicted initiation lives for the notched specimens.

A reason for the deviations in predictions could also have been that the critical distance for the material was not accurately determined, since it was adopted from a different alloy. Moreover, for higher load levels, the critical distance is known to increase compared to at the fatigue limit.⁵² A sensitivity analysis presented in Appendix C showed that doubling the value of d improved the fatigue predictions somewhat but had generally small impact except for on specimen 5.

6 | CONCLUSIONS

In the current work, a non-symmetric fatigue test on R4-grade steel performed at a stress amplitude just below the cyclic yield stress showed that the initial mean stresses relaxed by 49% during the half-life of the specimen. This proves that MSR is significant also at relatively low loads and should be considered in fatigue predictions.

The non-Masing behavior of R4-grade steel controlled the mean stress in the first load cycle.

Eight specimens with hemispherical notches were fatigue tested in a three-point bending setup. Fatigue initiation lives were predicted, using an R4-grade-steel $S-N$ curve compiled from the literature and taking into account the cyclic softening and MSR. This showed an improved accuracy over fatigue predictions based on the monotonic material model. Fatigue initiation locations were well predicted close to the mouths of the notches as measured by DIC. Good agreement between predicted and measured initiation lives was found for $N < 10^5$ cycles. For longer initiation lives, deviations were overly conservative. The deviations were likely caused by scatter in the $S-N$ data and residual machining stresses in the notches. A single value was used for the critical distance, independent on the load level. More accurate predictions are expected if a load dependent critical distance value is used.

Although the experimental data is limited, the current results show that MSR has a significant influence on fatigue initiation life in R4 steel. The approach outlined here is able to improve predictions in the finite life regime.

ACKNOWLEDGEMENTS

The authors would like to thank C. Frugone (NTNU) for his efforts to set up the fatigue rig and communications with the DIC system. P. J. Haagenen, T. Auestad, E. Fagerholt, L. Sandviken, M. Aursand, and L. Viespoli (NTNU and SINTEF) are also acknowledged for helpful discussions. The authors are grateful for financial support for the work received through the project KPN Lifemoor (RCN contract No. 280705).

NOMENCLATURE

a	crack depth
b	negative slope of the Basquin curve
c	crack half-length
d	critical distance
E	elastic modulus
K	strain hardening coefficient
m	negative slope of the Coffin-Manson curve
N	number of cycles
N_f	fatigue life
N_i	fatigue crack initiation life
$N_{i,\text{measured}}$	measured fatigue crack initiation life
$N_{i,\text{predicted}}$	predicted fatigue crack initiation life
n	strain hardening exponent
R	stress ratio
R^2	coefficient of determination
R_L	load ratio
$R_{p0.2}$	yield stress

R_ε	strain ratio
r	ratio of $N_{i,\text{measured}}$ to $N_{i,\text{predicted}}$
t	thickness
x, y, z	axes of Cartesian coordinate system
ε	strain
ε_a	strain amplitude
ε'_f	$N = 0.5$ intercept of the Coffin-Manson curve
$\varepsilon_{\text{plastic}}$	plastic strain
σ	stress
σ_a	stress amplitude
σ'_f	$N = 0.5$ intercept of the Basquin curve
σ_m	mean stress
$\sigma_{m,1}$	mean stress at first load cycle
$\sigma_{m,\text{half-life}}$	mean stress at half-life
σ_{max}	maximum stress

AUTHOR CONTRIBUTIONS

Paul Qvale contributed to the conceptualization, methodology, software, formalAnalysis, investigation, dataCuration, writingOriginalDraft, and visualization. Ershad P. Zarandi contributed to the conceptualization, methodology, investigation, and writingReviewEditing. Alberto Arredondo contributed to the investigation and writingReviewEditing. Sigmund K. Ås contributed to methodology, investigation, writingReviewEditing, supervision, and FundingAcquisition. Bjørn H. Skallerud contributed to conceptualization, methodology, writingReviewEditing, supervision, and fundingAcquisition.

DATA AVAILABILITY STATEMENT

The data that support the findings of this study are available from the corresponding author upon reasonable request.

ORCID

Paul Qvale  <https://orcid.org/0000-0002-7007-2865>

Sigmund K. Ås  <https://orcid.org/0000-0003-2690-0851>

REFERENCES

- Zarandi EP, Skallerud BH. Cyclic behavior and strain energy-based fatigue damage analysis of mooring chains high strength steel. *Mar Struct.* 2020;70:102703.
- Dowling NE. *Mechanical Behavior of Materials: Engineering Methods for Deformation, Fracture, and Fatigue.* 3rd ed. Upper Saddle River, NJ, USA: Pearson Prentice Hall; 2007.
- Schijve J. *Fatigue of Structures and Materials.* 2nd ed.: Springer Netherlands; 2009.
- Cofe NG, Krawinkler H. Uniaxial cyclic stress-strain behavior of structural steel. *J Eng Mech.* 1985;111(9):1105-1120.
- Ellyin F. Effect of tensile-mean-strain on plastic strain energy and cyclic response. *J Eng Mater Technol.* 1985;107(2):119-125.
- Jhansale HR, Topper TH. Engineering analysis of the inelastic stress response of a structural metal under variable cyclic

- strains. In: Coffin LF, Krempl E, eds. *Cyclic Stress-Strain Behavior—Analysis, Experimentation, and Failure Prediction*. West Conshohocken, PA: ASTM International; 1971: 246-270.
7. James MR. Relaxation of residual stresses—an overview. In: Niku-Lari A, ed. *Residual Stresses*: Pergamon; 1987:349-365.
 8. Hu W, Wang CH, Barter S. Analysis of Cyclic Mean Stress Relaxation and Strain Ratchetting Behaviour of Aluminium 7050. DSTO-RR-0153, DSTO Aeronautical and Maritime Research Laboratory; 1999. <https://apps.dtic.mil/sti/citations/ADA367233>
 9. Koh SK, Stephens RI. Mean stress effects on low cycle fatigue for a high strength steel. *Fatigue Fract Eng Mater Struct*. 1991; 14(4):413-428.
 10. Chaboche J-L, Kanouté P, Azzouz F. Cyclic inelastic constitutive equations and their impact on the fatigue life predictions. *Int J Plast*. 2012;35:44-66.
 11. Frederick CO, Armstrong PJ. A mathematical representation of the multiaxial Bauschinger effect. *Mater at High Temp*. 2007; 24:1-26.
 12. Zhuang WZ, Halford GR. Investigation of residual stress relaxation under cyclic load. *Int J Fatigue*. 2001;23:31-37.
 13. Lee C-H, Do VNV, Chang K-H. Analysis of uniaxial ratcheting behavior and cyclic mean stress relaxation of a duplex stainless steel. *Int J Plast*. 2014;62:17-33.
 14. Abaqus/cae user's guide; 2017.
 15. Landgraf RW, Chernenkoff RA. Residual stress effects on fatigue of surface processed steels. In: Champoux RL, Underwood LH, Kapp JA, eds. *Analytical and Experimental Methods for Residual Stress Effects in Fatigue*. ASTM International; 1988:1-12.
 16. Skallerud B, Larsen PK. A uniaxial cyclic plasticity model including transient material behaviour. *Fatigue Fract Eng Mater Struct*. 1989;12(6):611-625.
 17. Gabrielsen O, Liengen T, Molid S. Microbiologically influenced corrosion on seabed chain in the north sea. In: Proceedings of the ASME 2018 37th international conference on ocean, offshore and arctic engineering. ASME; 2018: V003T02A045.
 18. Ma K, Gabrielsen O, Li Z, et al. Fatigue tests on corroded mooring chains retrieved from various fields in offshore West Africa and the North Sea. In: Proceedings of the ASME 2019 38th International Conference on Ocean, Offshore and Arctic Engineering, Vol. 3. ASME; 2019:V003T02A060.
 19. Qvale P, Zarandi EP, Ås SK, Skallerud BH. Digital image correlation for continuous mapping of fatigue crack initiation sites on corroded surface from offshore mooring chain. *Int J Fatigue*. 2021;151:106350.
 20. Benedetti M, Berto F, Le Bone L, Santus C. A novel strain-energy-density based fatigue criterion accounting for mean stress and plasticity effects on the medium-to-high-cycle uniaxial fatigue strength of plain and notched components. *Int J Fatigue*. 2020;133:105397.
 21. Wang CH, Rose LRF. Transient and steady-state deformation at notch root under cyclic loading. *Mech Mater*. 1998;30(3): 229-241.
 22. Martinez Perez I, Constantinescu A, Bastid P, Zhang Y-H, Venugopal V. Computational fatigue assessment of mooring chains under tension loading. *Eng Fail Anal*. 2019;106:104043.
 23. Zarandi EP, Skallerud BH. Experimental and numerical study of mooring chain residual stresses and implications for fatigue life. *Int J Fatigue*. 2020;135:105530.
 24. Masing G. Eigenspannungen und Verfestigung beim Messing. In: Proceedings of the Second International Congress for Applied Mechanics; 1926:332-335.
 25. Offshore standards, DNV-OS-E302, offshore mooring chain. DNV-OS-E302, DNV AS; 2021.
 26. Zarandi EP. Multiaxial fatigue analysis of offshore mooring chains, considering the effects of residual stresses and corrosion pits. *Ph.D. thesis*: Trondheim, Norway: NTNU; 2020. <https://hdl.handle.net/11250/2686419>
 27. Neuber H. Theory of stress concentration for shear-strained prismatical bodies with arbitrary nonlinear stress-strain law. *J Appl Mech*. 1961;28(4):544-550.
 28. Basquin OH. The exponential law of endurance tests. *Am Soc Testing Mater Proc*. 1910;10:625-630.
 29. Coffin LF. A study of the effects of cyclic thermal stresses on a ductile metal. *Trans ASME*. 1954;76:931-950.
 30. Manson SS. Behavior of Materials Under Conditions of Thermal Stress. NACA-TN-2933, National Advisory Committee of Aeronautics; 1953.
 31. Smith KN, Topper T, Watson P. A stress-strain function for the fatigue of metals. *J Mater*. 1970;5:767-778.
 32. Härkegård G, Halleraker G. Assessment of methods for prediction of notch and size effects at the fatigue limit based on test data by Böhm and Magin. *Int J Fatigue*. 2010;32(10):1701-1709.
 33. Skallerud B, Ås SK, Ottosen NS. A gradient-based multiaxial criterion for fatigue crack initiation prediction in components with surface roughness. *Int J Fatigue*. 2018;117:384-395.
 34. Taylor D, Bologna P, Bel Knani K. Prediction of fatigue failure location on a component using a critical distance method. *Int J Fatigue*. 2000;22(9):735-742.
 35. Taylor D. Geometrical effects in fatigue: a unifying theoretical model. *Int J Fatigue*. 1999;21(5):413-420.
 36. Ahangarani S, Sabour AR, Mahboubi F. Surface modification of 30CrNiMo8 low-alloy steel by active screen setup and conventional plasma nitriding methods. *Appl Surf Sci*. 2007;254(5): 1427-1435.
 37. Prohaska M, Panzenboeck M, Anderl H, Kordasch W. Influence of chemical composition and microstructural parameters on speed of sound of various materials used for high-pressure applications. In: 18th World Conference on Nondestructive Testing; 2012:16-20. <https://www.ndt.net/search/docs.php?id=12709>
 38. Bruun ØA, Härkegård G. A comparative study of design code criteria for prediction of the fatigue limit under in-phase and out-of-phase tension-torsion cycles. *Int J Fatigue*. 2015;73:1-16.
 39. Arredondo A, Fernández J, Silveira E, Arana JL. Corrosion fatigue behavior of mooring chain steel in seawater. In: International Conference on Offshore Mechanics and Arctic Engineering, Volume 1: Offshore Technology; Offshore Geotechnics; 2016:V001T01A006.
 40. Pollak RD, Palazotto AN. A comparison of maximum likelihood models for fatigue strength characterization in materials exhibiting a fatigue limit. *Probabilistic Eng Mech*. 2009;24(2): 236-241.
 41. Wormsen A, Härkegård G. Weibull fatigue analysis of notched components under constant and variable amplitude loading.

- In: Proceedings of the 9th International Fatigue Congress 2006. Elsevier; 2006.
42. Jones EMC, Iadicola MAE. A good practices guide for digital image correlation; 2018.
43. Evans C, Leiva-Garcia R, Akid R. Strain evolution around corrosion pits under fatigue loading. *Theor Appl Fract Mech.* 2018; 95:253-260.
44. Raju IS, Newman JC, Atluri SN. Crack-mouth displacements for semielliptical surface cracks subjected to remote tension and bending loads. In: Atluri SN, Raju IS, Newman JC, Epstein JS, eds. In: *Fracture Mechanics: Twenty-Second Symposium (Volume II)*. Philadelphia: ASTM International; 1992:19-28.
45. Cerit M, Genel K, Eksi S. Numerical investigation on stress concentration of corrosion pit. *Eng Fail Anal.* 2009;16(7):2467-2472.
46. Jie Z, Susmel L. High-strength steel wires containing corrosion pits: Stress analysis and critical distance based fatigue life estimation. *Fatigue Fract Eng Mater Struct.* 2020;43(8):1611-1629.
47. Ding W, Zhang L, Li Z, Zhu Y, Su H, Xu J. Review on grinding-induced residual stresses in metallic materials. *Int J Adv Manuf Technol.* 2017;88:2939-2968.
48. El-Khabeery MM, Fattouh M. Residual stress distribution caused by milling. *Int J Mach Tools Manuf.* 1989;29(3):391-401.
49. Ma Y, Feng P, Zhang J, Wu Z, Yu D. Prediction of surface residual stress after end milling based on cutting force and temperature. *J Mater Process Technol.* 2016;235:41-48.
50. Nespor D, Denkena B, Grove T, Böß V. Differences and similarities between the induced residual stresses after ball end milling and orthogonal cutting of Ti-6Al-4V. *J Mater Process Technol.* 2015;226:15-24.
51. Lassen T, Storvoll E, Bech A. Fatigue life prediction of mooring chains subjected to tension and out of plane bending. In: International Conference on Offshore Mechanics and Arctic Engineering, Vol. Volume 1: Offshore Technology; 2009:229-239.
52. Benedetti M, Santus C. Statistical evaluation of the critical distance in the finite life fatigue regime. *Procedia Struct Integr.* 2020;28:702-709. 1st Virtual European Conference on Fracture - VECF1.

How to cite this article: Qvale P, Zarandi EP, Arredondo A, Ås SK, Skallerud BH. Effect of cyclic softening and mean stress relaxation on fatigue crack initiation in a hemispherical notch. *Fatigue Fract Eng Mater Struct.* 2022;1-17. doi:[10.1111/ffe.13834](https://doi.org/10.1111/ffe.13834)

APPENDIX A: FRACTURE SURFACES

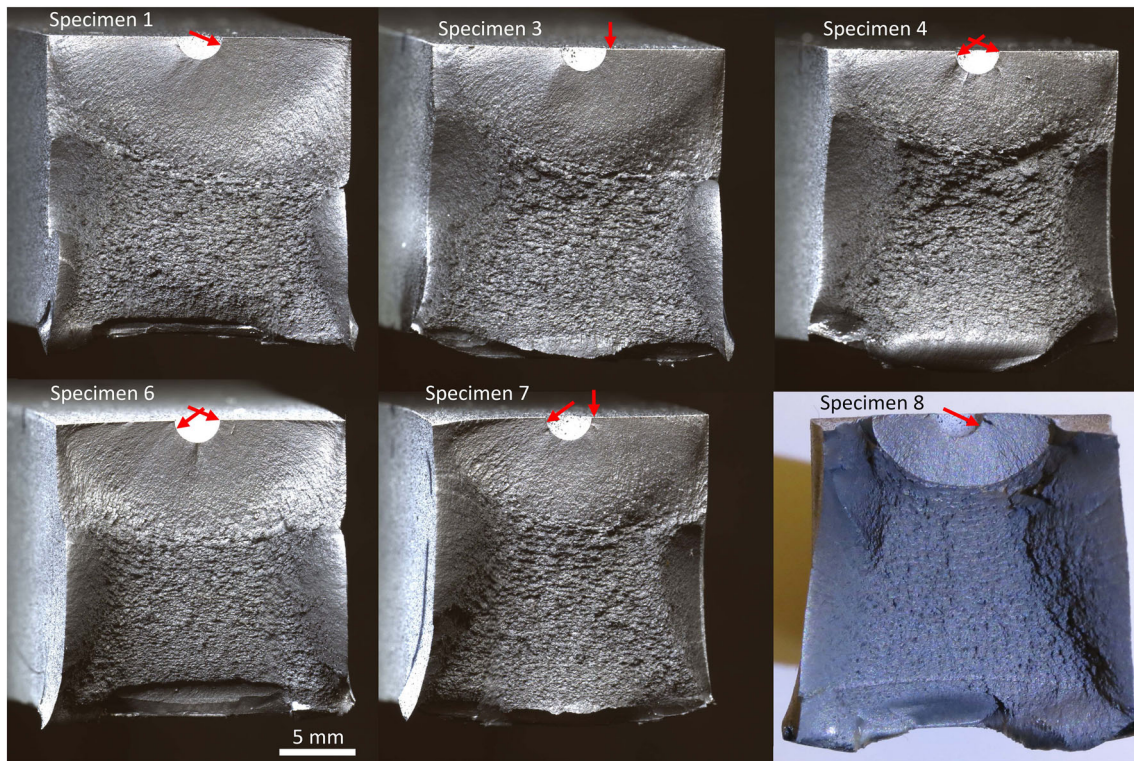


FIGURE A1 Micrographs of fracture surfaces of all notched specimens where cracks initiated. Red arrows mark initiation sites detected by DIC. Fatigue testing of specimen 8 was terminated before final fracture, in order to perform a separate study [Colour figure can be viewed at wileyonlinelibrary.com]

APPENDIX B: TABLE OF FATIGUE INITIATION LIVES

TABLE B1 Comparison between predicted and measured fatigue initiation lives

Specimen ID	1	2	3	4	5	6	7	8
Preloaded	Yes	Yes	Yes	Yes	No	No	No	No
Load amplitude (kN)	8	8	10	12	8	10	12	14
Mean load (kN)	12	12	15	18	12	15	18	21
$N_{i,measured}$	359,600	(1,653,300)	27,200	12,200	(1,527,610)	54,900	16,700	5800
N_f	421,328	-	64,920	33,452	-	93,605	39,687	(18,554)
Runout	No	Yes	No	No	Yes	No	No	After initiation
Values of $r = N_{i,predicted} / N_{i,measured}$								
Cyclic + MSR	0.11	0.02	0.41	0.51	0.26	0.38	0.39	0.88
Cyclic	0.11	0.03	0.41	0.37	0.26	0.38	0.36	0.46
Monotonic	0.04	0.01	0.22	0.26	0.11	0.17	0.20	0.35

Note: Cycle numbers in parentheses mark the counts when fatigue testing was ended in run-out tests.

APPENDIX C: SENSITIVITY ANALYSIS ON CRITICAL DISTANCE

To investigate the sensitivity of the fatigue predictions to the critical distance, a sensitivity analysis was performed, where d was doubled from 34 to 68 μm . The results in

Figure C1 show generally low impact on predictions, although accuracy improves slightly for all specimens. The increase in d has, however, a large effect on the maximum stresses in the notch of specimen 5, which is characterized by largely elastic stress cycling up from a highly compressive residual stress. Thus, fatigue predictions are greatly affected.

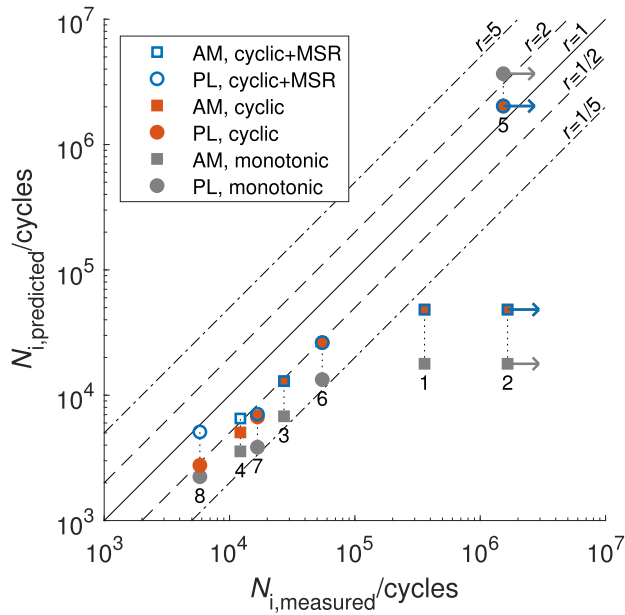


FIGURE C1 Predicted versus measured initiation lives for the notched specimens, if doubling the critical distance to $d = 68 \mu\text{m}$ [Colour figure can be viewed at wileyonlinelibrary.com]